ResearchGate

See discussions, stats, and author profiles for this publication at: https://www.researchgate.net/publication/5573018

Molecular Dynamics Simulation of Thermomechanical Properties of Montmorillonite Crystal. 1. Isolated Clay Nanoplate

ARTICLE *in* THE JOURNAL OF PHYSICAL CHEMISTRY B · APRIL 2008

Impact Factor: 3.3 · DOI: 10.1021/jp076022q · Source: PubMed

CITATIONS
20

READS
103

7 AUTHORS, INCLUDING:

Mikhail Abramovich Mazo
Semenov Institute of Chemical Physics
50 PUBLICATIONS **334** CITATIONS
SEE PROFILE

Alexander Alexandrovich Berlin
Russian Academy of Sciences
399 PUBLICATIONS **716** CITATIONS
SEE PROFILE

Nikolay K. Balabaev
Russian Academy of Sciences
133 PUBLICATIONS **948** CITATIONS
SEE PROFILE

Available from: Mikhail Mazo
Retrieved on: 25 January 2016

Molecular Dynamics Simulation of Thermomechanical Properties of Montmorillonite Crystal. 1. Isolated Clay Nanoplate

Mikhail A. Mazo,*,† Leonid I. Manevitch,† Elena B. Gusarova,† Mikhail Yu. Shamaev,† Alexander A. Berlin,† Nikolay K. Balabaev,‡ and Gregory C. Rutledge§

Semenov Institute of Chemical Physics, Russian Academy of Science, Kosygin Street 4, Moscow 119991, Russia, Institute of Mathematical Problems of Biology, Russian Academy of Science, Pushchino 142290, Russia, and Department of Chemical Engineering, Massachusetts Institute of Technology, Cambridge, Massachusetts 02139

Received: July 30, 2007; In Final Form: November 28, 2007

The structure and mechanical properties of clay nanoparticles is a subject of growing interest because of their numerous applications in engineering. We present the results of molecular dynamics simulation for a single nanoplate of pyrophyllite − a 2:1 clay mineral consisting of two tetrahedral sheets of SiO_4 and an intervening octahedral AlO_6 sheet. Simulations were performed in the temperature interval from 5 to 750 K using the ionic-type potentials of Cygan et al. On this basis the temperature dependences of structural parameters, characterizing both tetrahedral and octahedral sheets as well as single lamella, have been studied. Two slightly different structures were observed in this wide temperature interval. The mechanical properties of the nanoplate were calculated from stress−strain diagrams, which have been obtained at relatively slow rates of deformation (for molecular simulations). Using different types of loading, we calculated the full elasticity tensor and estimated the influence of temperature on its components. We estimated also the bending and torsion stiffnesses of the nanoplate as specific characteristics of this type of particle. Because the nanoplate is atomically thin, a reasonable determination of the thickness is a nontrivial problem, both in the modeling of mechanical properties and in physical interpretation of the obtained data. We propose a procedure for its calculation.

1. Introduction

The properties of smectite clay minerals are actively studied now because they are important in a number of technological and biochemical processes such as catalytic activity, filtration of fluids, and waste disposal.[1,2] Like all clay minerals, smectites are aluminum phyllosilicates. The structure of this crystal is composed of two silicate tetrahedral sheets sandwiching one aluminum− or magnesium−oxygen−hydroxyl octahedral sheet. These three sheets are packaged into layers having a thickness on the order of 1 nm and lateral (in-plane) dimensions of 100−1000 nm. Such nanoplates tend to form microscopic to submicroscopic crystals, with water and cations in the interlayer.

Because clay minerals are not perfect crystals as a rule, their experimental study is a rather complicated problem, as is that of a single lamella. It requires, in particular, X-ray refinement studies using large single crystals. Therefore, only a few detailed structural characterizations exist for such clays. Additionally, clay minerals frequently lack long-range order, in particular with respect to the stacking behavior of the clay layers.

In recent years these minerals attracted attention in connection with construction of a new class of composite materials−polymer−clay nanocomposites. It turned out that a polymer matrix filled with exfoliated clay layers demonstrated unique regularities for a number of composite properties, among them mechanical reinforcement and barrier properties.[3] In this connection estimation of thermophysical and mechanical properties of clay nanoplates is one of the key problems in this field. Besides, a variety of multicomponent substitutions in the tetrahedral and octahedral sheets are possible that lead to specific chemistries.

In this situation molecular computer simulations, molecular dynamics (MD) and Monte Carlo, have become very useful for study of the structure and physical properties of clay minerals. Now these methods are successfully applied for investigation of the structure of both crystalline layers and the interlayer space and swelling behavior of smectite clays,[4−10] but application of molecular simulation methods requires the use of a reliable force field.

Several well-grounded potentials have been proposed to date. The development of the bond potential by Teppen et al.[11] allows a crystalline structure of clay minerals to be modeled with good accuracy. However, the metal atoms and to some extent those of oxygen possess an ionic form. This peculiarity leads to essential difficulties if considering purely bonded forces. To overcome these difficulties, Sainz-Diaz et al.[12] suggested an alternative force field, in which covalent effects were simulated using three-body bond-bending interactions. However, formal charges on metals and structural oxygens may still not be accurate for simulating sorption and other surface phenomena.

The empirical CLAYFF force field[13] was used to compute the energy of the system, including the angle bend term for hydroxyl groups. This force field has been shown to reproduce

* To whom correspondence should be addressed. Fax: (7495)-137-8284. E-mail: mazo@polymer.chph.ras.ru.
† Semenov Institute of Chemical Physics, Russian Academy of Science.
‡ Institute of Mathematical Problems of Biology, Russian Academy of Science.
§ Massachusetts Institute of Technology.

10.1021/jp076022q CCC: $40.75 © 2008 American Chemical Society
Published on Web 02/16/2008

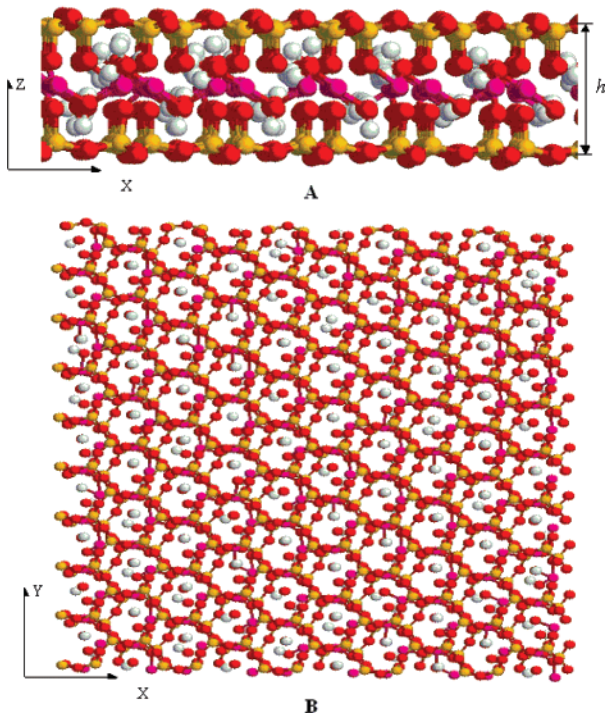

Figure 1. Structure of a simulated pyrophyllite nanoplate: (A) projection view along the *y* direction (fragment); (B) projection view along the *z* direction (computational cell).

the bulk crystal structure of a number of different clays, as well as the vibrational spectrum of hydrotalcite[13] and pyrophyllite.[14]

In this work we chose one layer of pyrophyllite crystal for study of the affect of temperature on the structure and mechanical properties of the nanoplate, which in turn is important for prediction of nanocomposite properties.[15,16] Earlier we used a bonded force field for calculation of the mechanical properties of one such nanocrystal at room temperature, but there we chose only to report elastic properties in a form that was independent of the value taken for nanoplate thickness.[17] Now we can calculate this tensor, and moreover, we have studied the behavior of the nanoplate at different temperatures.

2. Model and Simulation Details

The system under consideration is a single clay lamella of pyrophyllite-1Tc; the corresponding chemical formula is $[Al_2Si_4O_{10}(OH)_2]_2$ for the crystallographic unit cell. The natural clay lamella consists of only one crystallographic unit cell in the thickness direction and has much larger prolongation in the other two directions (100−1000 nm). Our computational cell forms a parallelepiped (except when shear deformation is modeled in the lamella plane) with initial dimensions $L_x = 4.64$ nm, $L_y = 4.48$ nm, and $L_z = 5.00$ nm and periodic boundary conditions in all three directions (Figure 1). The clay lamella was oriented parallel to the *xy* plane, and the computational cell consisted of 45 unit cells (1800 atoms), 9 cells being situated along the *y* direction (*a* axis of the unit cell) and 5 along the *x* direction (*b* axis of the unit cell). We studied the size effects by considering simulation cells made up of 15, 45, 60, 90, and 180 crystallographic unit cells for calculation of the elasticity coefficients of lamella in the *a* and *b* directions, but did not see any noticeable distinctions. The period in the *z* direction was chosen as 5 nm, so that interaction between the simulated clay sheet and its images was negligible. This expediency allowed us to use our 3D periodic computer code for simulated 2D periodic lamella. The size of the computational cell was the same in all calculations.

The empirical CLAYFF force field[13] was used to compute the energy of the system, including the angle bend term for hydroxyl groups. The long-range Coulombic interactions were calculated using a smooth particle Ewald method.[18] We simulated the system by MD using the program PUMA.[19] Collisional dynamics[20] was used to maintain isothermal conditions, and Berendsen's barostat was used to maintain the stress constant.[21] The corrections were applied to prevent the rotation and translation of the system as a whole. The integration time step was 0.001 ps. The initial coordinates of the clay atoms were generated using the data of Wardle and Brindley.[22]

The system was first equilibrated at 300 K for 100 ps at atmospheric pressure. Stepwise cooling and heating with steps of 50 K followed by an equilibration of 50−100 ps duration were performed before production runs were carried out. However, we have revealed a transition into another state with a lower potential energy when the temperature reached 450 K, and this new state remained stable for temperatures from 5 to 750 K. When dealing with calculation of the mechanical properties, the initial data (coordinates and velocities) corresponded to the state with a lower energy.

3. Results and Discussion

3.1. Crystal Structure. The temperature dependences of the lattice parameters *a* and *b* as well as nanoparticle thickness *h* and potential energy U_{pot} are shown in Figure 2. All magnitudes were calculated in the equilibrium state by time averaging over 50 ps. As this takes place, we found *a* and *b* using the values L_x and L_y. For purposes of Figure 2, the thickness *h* was calculated as the difference between average values of *z* projections of mass centers of the basal oxygen atoms at opposite sides of the lamella.[17]

The calculated parameters of the crystal are in close agreement with the experimental data ($a = 5.161$ nm, $b = 8.958$ nm, and $h = 6.947$ nm[22] and $a = 5.160$ nm, $b = 8.966$ nm, and $h = 6.999$ nm;[23] the experimental values of *h* were calculated according to coordinates of atoms presented in the mentioned papers). We can see that this thickness decreases linearly with decreasing temperature. The calculated coefficients of thermal expansion (CTEs) in the *a* and *b* directions for both states are nearly equal: $K_{T,a} = (1.01 \pm 0.01) \times 10^{-5}$ K^{-1}, $K_{T,b} = (1.03 \pm 0.01) \times 10^{-5}$ K^{-1}, whereas in the *z* direction $K_{T,h} = (1.54 \pm 0.03) \times 10^{-5}$ K^{-1}. Therefore, a noticeable anisotropy of thermal expansion can be observed due to larger mobility of the system in the *z* direction. We present the equilibrium lattice parameters for three temperatures in Table 1.

Because the crystal under consideration consists of three sheets (two silicate tetrahedral sheets and one aluminum octahedral sheet), it is interesting to calculate the CTEs of these sheets in the *z* direction, in which they can be almost independently extended. Analogously to the definition of *h*, we have introduced the thickness h_t of the tetrahedral sheets and the thickness h_o of the octahedral sheet, dividing the pyrophyllite lamella by two planes passing through the centers of mass of the apical oxygen atoms. It turned out that the thicknesses h_t and h_o are similar in magnitude and depend linearly on temperature: $h_t = (0.21 + 1.0 \times 10^{-6} \times T)$ nm, $h_o = (0.23 + 0.74 \times 10^{-6} \times T)$ nm. The corresponding CTEs are $K_{T,h,t} = 0.5 \times 10^{-5}$ K^{-1} for the tetrahedral sheets and $K_{T,h,o} = 3.2 \times 10^{-5}$ K^{-1} for the octahedral sheet. It is seen that the predominant contribution to the CTE of the lamella is made by the octahedral sheet.

As seen from Figure 3, the average values of the bond lengths in both states of the nanoplate are close. Their difference is near 0.7−0.8% in the octahedra but is significantly less (∼0.1%)

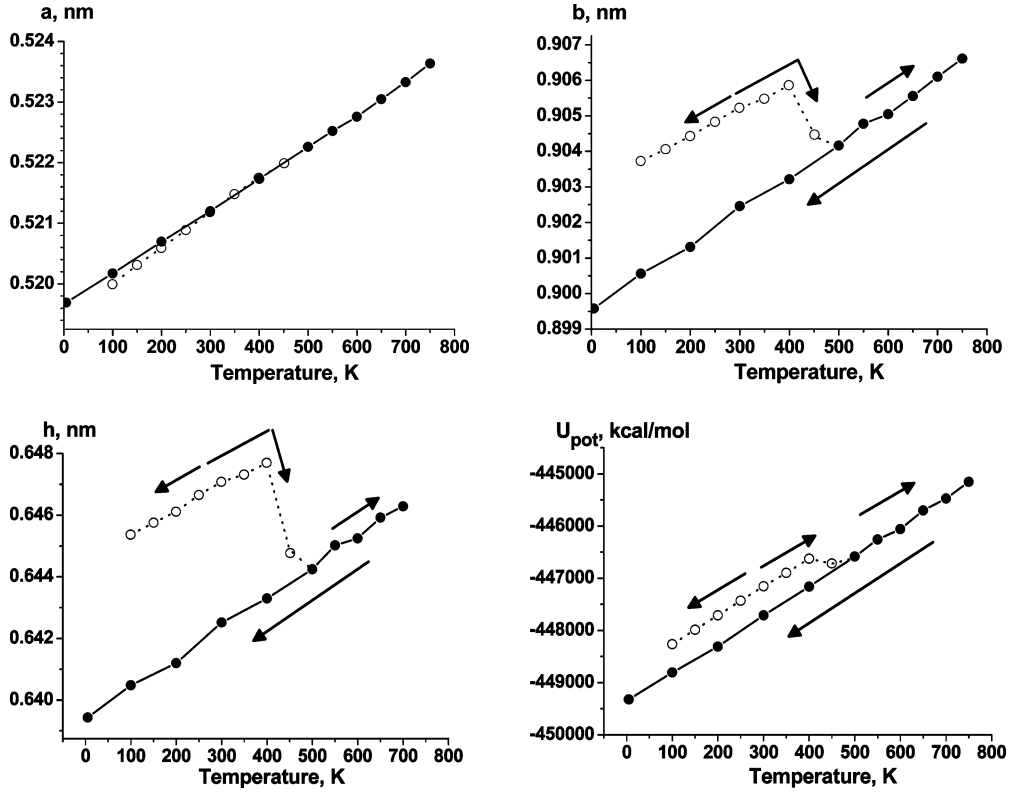

Figure 2. Temperature dependences of the lattice parameters *a* and *b* and the thickness of the plate *h*. Open and closed circles correspond to quasi-equilibrium and equilibrium states, respectively. The direction of temperature change in the calculations is shown by arrows, starting at 300 K in the quasi-equilibrium state.

TABLE 1: Equilibrium Lattice Parameters *a* and *b* and the Thickness of the Plate *h* for Three Temperatures at Which the Elasticity Tenser Was Calculated

temp, K	*a*, nm	*b*, nm	*h*, nm
100	$0.5202 \pm 1 \times 10^{-4}$	$0.9006 \pm 1 \times 10^{-4}$	$0.6405 \pm 1 \times 10^{-4}$
300	$0.5212 \pm 2 \times 10^{-4}$	$0.9024 \pm 3 \times 10^{-4}$	$0.6425 \pm 1 \times 10^{-4}$
700	$0.5233 \pm 3 \times 10^{-4}$	$0.9061 \pm 6 \times 10^{-4}$	$0.6463 \pm 1 \times 10^{-4}$

in the tetrahedra. The CTE for all valence bonds (except the hydroxyl) is approximately $(1.5-1.6) \times 10^{-5}$ K^{-1} and is close to $K_{T,h}$. At the same time, the CTE for the valence bond Al−OH is significantly larger ($\sim 2.6 \times 10^{-5}$ K^{-1}). The observed states are not significantly different; however, the existence of two states seems to be interesting.

The thermal capacity C_p of the nanoplate may be calculated using the formula

$$C_p = \frac{dU_{pot}}{dT} + p\frac{dV}{dT} \quad (1)$$

where p and V are the external pressure and volume of the crystal, respectively. The second term in eq 1 is significantly less than the first one, and it has not been taken into account. For both forms of the nanocrystal, the temperature dependence of U_{pot} is linear and C_p is equal to 0.172 kcal kg^{-1} K^{-1}.

3.2. Calculation of the Components of the Elasticity Tensor. Hereinafter for brevity, we use Voigt notation.[24] The components of the elasticity tensor C_{ij} and the components of its inverse, the compliance tensor, S_{ij} are written as 6×6 matrices and have in general 21 independent components. To determine the components of the elasticity tensor, we have performed six deformation simulations by application of the corresponding tensile and shear deformations. The rates of the deformations were small enough to exclude the rate dependence of the results: calculated values differed by 5−6% when the rate of deformation was reduced by a factor of 10.

When the deformation was performed along the *a* axis, the corresponding size of the computational cell in the *x* direction was changed with a constant rate and atmospheric pressure was maintained along the *b* axis. Because the computational cell was constrained to remain rectangular in the *ab* plane (i.e., $\epsilon_6 = 0$), the corresponding shear stress σ_6 can be nonzero. In this case we obtained six relations:

$$\epsilon_i = S_{i1}\sigma_1 + S_{i6}\sigma_6 \; (i = 1, 2, ..., 6) \quad (2)$$

where ϵ_i, σ_1, and σ_6 were measured during the MD experiments. The same calculations were performed for deformation in the direction of the *b* axis. In this case we have

$$\epsilon_i = S_{i2}\sigma_2 + S_{i6}\sigma_6 \; (i = 1, 2, ..., 6) \quad (3)$$

For analyzing the response of the crystal caused by deformation of the angle between the *x* and *y* directions, we changed the corresponding angle of the computational cell. This allows the following six relations to be obtained:

$$\epsilon_i = S_{i6}\sigma_6 \; (i = 1, 2, ..., 6) \quad (4)$$

To determine the elastic properties in the *z* direction, we introduced the external forces $\vec{f}_i^{(1)}$ and $\vec{f}_i^{(2)}$ of equal magnitudes but opposite directions, which were applied in the normal direction to all the oxygen atoms located at each surface of the lamella, similar to our earlier paper.[17] The corresponding external stress can be presented as follows:

$$P_3 = \frac{1}{2L_xL_y}\left(\sum\left|\vec{f}_i^{\rho(1)}\right| + \sum\left|\vec{f}_i^{\rho(2)}\right|\right) \quad (5)$$

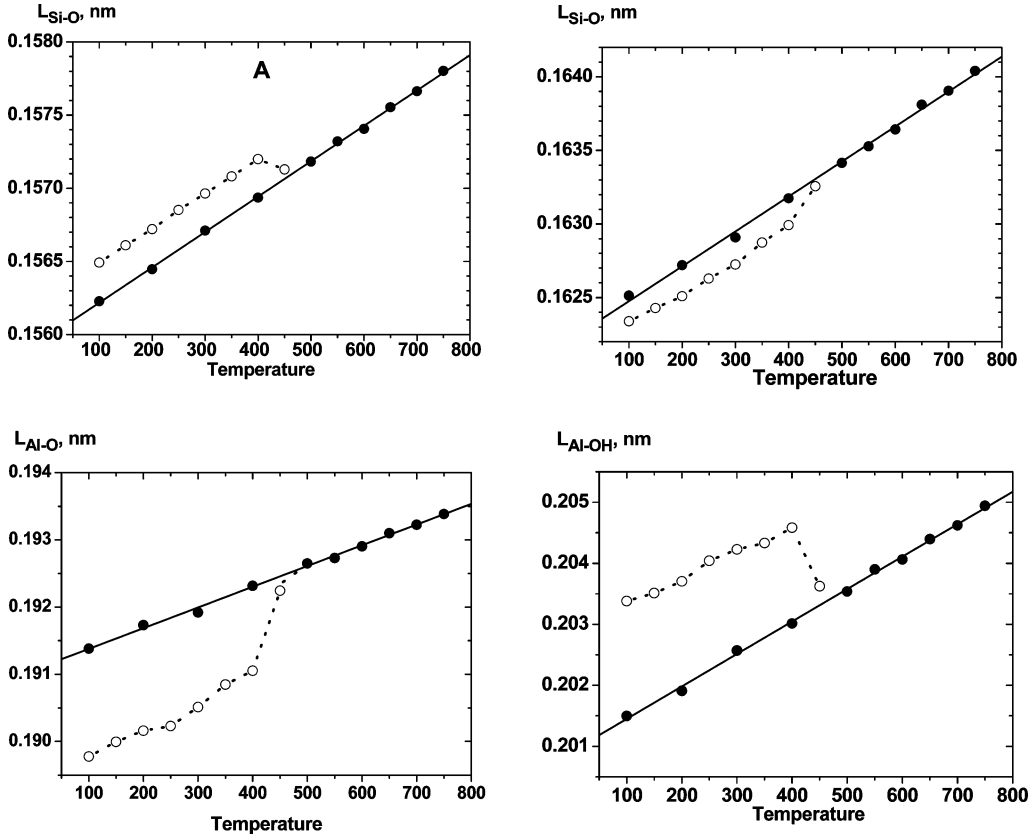

Figure 3. Temperature dependences of the bond lengths in pyrophyllite. The notations are similar to those in Figure 2.

TABLE 2: Strain Rates in MD Simulation

variable parameter	strain rate
ϵ_1	$d\epsilon_1/dt = 3.2 \times 10^6\ s^{-1}$; $d\epsilon_1/dt = 3.2 \times 10^5\ s^{-1}$
ϵ_2	$d\epsilon_2/dt = 3.2 \times 10^6\ s^{-1}$; $d\epsilon_2/dt = 3.2 \times 10^5\ s^{-1}$
P_3	$d\epsilon_3/dt = 3.0 \times 10^7\ s^{-1}$; $d\epsilon_3/dt = 3.0 \times 10^6\ s^{-1}$ [a]
P_4	$d\epsilon_4/dt = 1.3 \times 10^{-4}$ rad/ps; $d\epsilon_4/dt = 1.2 \times 10^{-5}$ rad/ps[a]
P_5	$d\epsilon_5/dt = 1.1 \times 10^{-4}$ rad/ps; $d\epsilon_5/dt = 1.2 \times 10^{-5}$ rad/ps[a]
ϵ_6	$d\epsilon_6/dt = 1.0 \times 10^{-3}$ rad/ps; $d\epsilon_6/dt = 1.0 \times 10^{-4}$ rad/ps

[a] In this case, dP/dt was given a constant value and $d\epsilon/dt$ was calculated.

The similar external forces directed along the x or y direction induced the shearing stresses P_4 and P_5, so that we obtain another 18 relations:

$$\epsilon_i = S_{i3}P_3 + S_{i6}\sigma_6\ (i = 1, 2, ..., 6) \quad (6)$$

$$\epsilon_i = S_{i4}P_4 + S_{i6}\sigma_6\ (i = 1, 2, ..., 6) \quad (7)$$

$$\epsilon_i = S_{i5}P_5 + S_{i6}\sigma_6\ (i = 1, 2, ..., 6) \quad (8)$$

All 36 components of S_{ij} can be calculated by solution of the system of eqs 2−4 and 6−8. Then we find the components of the elasticity tensor $C_{ij} = S_{ij}^{-1}$. Some additional details of these calculations are presented in Table 2. Because we deal with linear elasticity, the deformations are suggested to be small enough (they did not exceed 1% and 5% for low and high deformation rates, respectively).

The components of the stress tensor σ_{ik}^* were calculated in MD simulation using the virial theorem:[25]

$$\sigma_{jk}^* = (1/V)\{Nk_BT\delta_{jk} + \langle W_{jk}\rangle\} \quad (9)$$

TABLE 3: Components of the Elasticity Tensor Calculated at Different Temperatures (GPa)

T, K	C_{11}	C_{22}	C_{33}	C_{44}	C_{55}	C_{66}
100	470	437	268	56	73	127
300	442	399	253	54	70	120
700	413	381	229	50	65	113

	C_{12}/C_{21}	C_{13}/C_{31}	C_{23}/C_{32}	C_{45}/C_{54}	C_{46}/C_{64}	C_{56}/C_{65}
100	229/224	41/34	41/30	4/3	−10/−12	2/2
300	200/200	38/39	40/44	4/4	−12/−10	−1/2
700	185/184	38/37	42/47	2/0	−10/−10	0/1

	C_{14}/C_{41}	C_{15}/C_{51}	C_{16}/C_{61}	C_{24}/C_{42}	C_{25}/C_{52}	C_{26}/C_{62}
100	1/2	34/33	−2/−3	−1/−1	2/1	−1/−2
300	2/2	33/33	−6/−4	0/0	1/4	−3/−2
700	0/1	31/38	0/−2	0/1	1/16	0/−1

	C_{34}/C_{43}	C_{35}/C_{53}	C_{36}/C_{63}
100	−2/−2	43/42	2/2
300	2/−1	38/38	−1/3
700	0/1	31/33	0/−1

where $\langle W_{jk}\rangle$, V, N, k_B, T, and δ_{jk} are the "internal virial" averaged over time, the volume of the computational cell, the number of atoms, Boltzmann's constant, the temperature, and the Kronecker symbol, respectively.

However, in our case the plate occupies only part of the computational cell ($V_{lam}/V = h/L_z$, where V_{lam} is the volume of the lamella and h is the yet unknown thickness of the lamella). Therefore, one cannot estimate exactly the internal stresses without some additional piece of information.[17] Equality of the internal (eq 9) and external (eq 5) stresses allows one to calculate an effective thickness of the lamella. These stresses are proportional to each other for all temperatures, and the effective thickness turns out to be very close to the thickness of the plate h. Only in two cases the deviations are close to 2% and 1.5%,

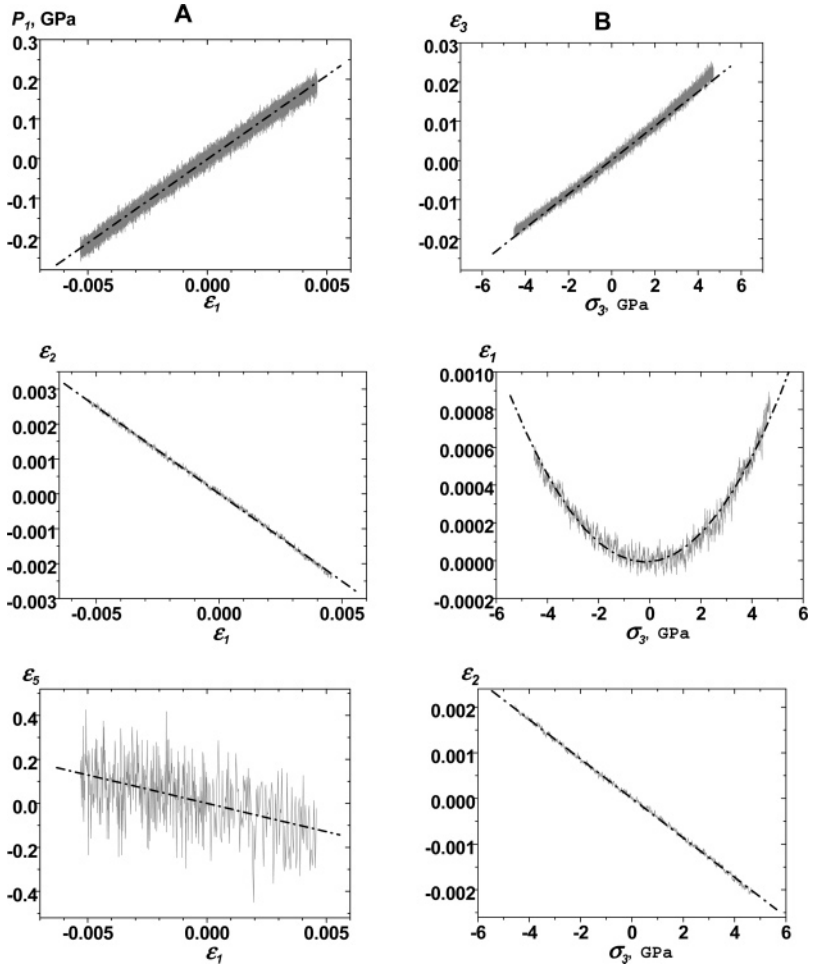

Figure 4. Results of MD simulation of unidirectional deformation along the *a* axis (A) and transverse to the plane sheet (B).

TABLE 4: Bending and Torsion Constants (10^{-17} N m)

temp, K	D_1	D_2	D_3
100	1.38	1.28	0.278
300	1.29	1.16	0.265
700	1.19	1.10	0.254

and were no more than 0.5% in all other simulations. Therefore, we have used the values of h for calculation of genuine internal stresses. Because S_{ij} and C_{ij} have to be symmetric, their symmetry is a good test of the accuracy of the calculations and for the estimation of the thickness h. It is worth mentioning that further decreasing the deformation rate results in increasing the fluctuations of the deformation tensor and thereby decreasing the accuracy of the calculations.

The results of MD simulations of unidirectional deformation along the *a* axis and in the *z* direction are shown in Figure 4. As seen from Figure 4A, a linear dependence of σ_1, ϵ_2, and ϵ_5 on ϵ_1 is observed for $|\epsilon_1| < 0.05$, which allows determination of the slope of these curves with good accuracy. More complicated behavior is typical for deformation of the pyrophyllite crystal along the *z* axis (Figure 4B). In this case one can see a linear dependence of ϵ_2 on P_3 for $|\epsilon_3| < 0.04$, but noticeable deviations from linearity are observed for the dependence of ϵ_3 on P_3 for $|\epsilon_3| > 0.01$ and dependence of ϵ_1 on P_3 (this dependence is quadratic: both increasing and decreasing the thickness result in very small increases in the *a* dimension). The quadratic dependences are obtained also for ϵ_1 and ϵ_2 in the case of shear deformation along the *b* axis.

TABLE 5: Elastic Properties of Pyrophyllite Lamella at 300 K

	ref 17		this work
	$N = 288$, strain rate 1.5×10^{-3} m/s	$N = 288$, strain rate 1.5×10^{-4} m/s	$N = 1800$, strain rate 1.5×10^{-3} m/s
E_1h (N/m)	261	259	284
E_2h (N/m)	229	249	256
E_3h (N/m)	239		163
E_4h (N/m)	66.4		35
E_5h (N/m)	162		45
E_6h (N/m)	170	167	77
ν_{12}	0.41	0.44	0.48
ν_{21}	0.45	0.49	0.50
ν_{31}	0.14		0
ν_{13}	0.14		0
ν_{32}	0.27	0.18	0.14
ν_{23}	0.27	0.17	0.1
D_1/h^2 (N/m)	26.7	27.9	29.0
D_2/h^2 (N/m)	24.7	26.8	25.4
D_3/h^2 (N/m)	14.1	14.1	6.4

We present calculated components of the elasticity tensor in Table 3 for three values of the temperature. It is worth mentioning that the tensors obtained are symmetric, to good accuracy (the only discrepancy is observed for C_{25} and C_{52} at 700 K). Diagonal components of the elasticity tensor are presented in the first line of Table 3. Although their magnitudes decrease with an increase of the temperature ($dC_{ii}/dT \approx -0.09$ Gpa K^{-1}), the relative values are almost the same: C_{11}:C_{22}:C_{33}:C_{44}:C_{55}:C_{66} = 1:0.92:0.57:0.12:0.16:0.27. The relationship among C_{11}, C_{22}, and C_{33} correlates well with the relative

magnitudes of CTEs $K_{T,a}$, $K_{T,b} < K_{T,h}$. The smaller value C_{33} and larger value α_h are determined by larger stiffnesses of tetrahedral sheets in comparison to octahedral ones. These sheets can be considered as sequentially connected springs in the *z* direction, while being connected in parallel in the *x* and *y* directions.

The magnitudes of bending and torsion constants for a single sheet of pyrophyllite were estimated using the theory of thin plates:[26]

$$D_1 = \frac{E_1 h^3}{12(1 - \nu_{12}\nu_{21})}, \quad D_2 = \frac{E_2 h^3}{12(1 - \nu_{12}\nu_{21})}, \quad D_3 = \frac{E_6 h^3}{12} \tag{10}$$

The results are presented in Table 4. Both bending stiffnesses have close magnitudes, torsion stiffness being almost 5 times smaller. It is interesting to compare the results obtained here with the elastic stiffnesses and Poisson coefficients calculated in ref 17 with use of the bonded force fields. Such comparison is presented in Table 5. One can see that both tensile moduli and Poisson coefficients in the *xy* plane are in close agreement with the corresponding values presented earlier;[17] however, other tensile and shear moduli as well as Poisson coefficients are smaller.

Since we used atomistic deformation of the isolated sheet, the obvious choice for *h* of an isolated sheet is the average distance *h* between opposing layers of oxygen atom centers at each surface of the sheet. However, for comparing our results with experimental data and results of computer simulation of clay crystals, it is necessary to take into account the real thickness of lamellae. For a corresponding discussion see previous works.[17,27]

4. Conclusion

The results of MD simulation of single pyrophyllite lamellae with the CLAYFF force field allow the following conclusions to be made.

(1) It is shown that two slightly different crystalline structures of a clay nanocrystal can be attained using different temperature regimes.

(2) The coefficients of thermal expansion of the single lamella are calculated, and the predominant contribution of octahedral layers to their magnitudes is revealed.

(3) All components of the elasticity tensor of a clay nanoplate are calculated, and their temperature behavior is analyzed.

(4) The temperature dependence of elasticity moduli is rather significant. As the temperature increases, the moduli decrease, but one observes almost proportional changes of all elastic characteristics.

(5) The data obtained with use of significantly different empirical potentials of interaction (the bonded and the ionic-type force fields) are in a close enough agreement if dealing with tensile (compression) or bending moduli in the *x* and *y* directions. As for the *z* direction, application of CLAYFF potentials leads to smaller magnitudes of both tensile (compressive) and shear moduli. The same is valid for the shear modulus in the *xy* plane. The relationship between E_1 (E_2) and E_3 that has been calculated in the present paper is in close accordance with our data for CTEs.

(6) The calculation of the full elasticity tensor has shown that the deflections from the case of orthothropic symmetry can be noticeable; the coefficients C_{15} and C_{35}, which are equal to zero for an orthotropic body, have magnitudes close to that of C_{44}.

Acknowledgment. This study was sponsored by the CRDF (Project RUC2-2626-MO-04). We are also grateful to Prof. P. Khalatur for useful discussion.

References and Notes

(1) Giese, R. F.; van Oss, C. J. *Surfactant Science Series 105*; Marcel Dekker: New York, 2002.
(2) *Reviews in Mineralogy. Vol. 19. Hydrous Phyllosilicates*; Baily, S. W., Ed.; 1988.
(3) Pinnavaia, T. J.; Beall, G. W. *Polymer-Clay Nanocomposites*; John Wiley and Sons: Chichester, U.K., 2000.
(4) Cygan, R. T. *Rev. Mineral. Geochem.* **2001**, *42*, 1.
(5) Greenwell, H. C.; Jones, W.; Coveney, P. V.; Stackhouse, S. *J. Mater. Chem.* **2006**, *16*, 708.
(6) Arab, M.; Bougeard, D.; Smirnov, K. S. *Phys. Chem. Chem. Phys.* **2004**, *6*, 2446.
(7) Ichikawa, Y.; Kawamura, K.; Theramast, N.; Kazumi, K. *Mech. Mater.* **2004**, *36*, 487.
(8) Satoru, S.; Katsuyuki, K. *J. Phys. Chem. B* **2004**, *108*, 13468.
(9) Kumar, P. P.; Kalinichev, A. G.; Kirkpatrick, R. J. *J. Phys. Chem. B* **2006**, *110* (9), 3841.
(10) Wang, J. W.; Kalinichev, A. G.; Kirkpatrick, R. J. *Geochem. Cosmochem. Acta* **2006**, *70*, 562.
(11) Teppen, B. J.; Rasmussen, K.; Bertsch, P. M.; et al. *J. Phys. Chem. B* **1997**, *101*, 1579.
(12) Sainz-Diaz, C. I.; Hernandez-Laguna, A.; Dove, M. T. *Phys. Chem. Miner.* **2001**, *28*, 130.
(13) Cygan, R. T.; Liang, J. J.; Kalinichev, A. G. *J. Phys. Chem. B* **2004**, *108*, 1255.
(14) Kalra, A.; Parks, D. M.; Rutledge, G. C. *Macromolecules* **2007**, *40*, 140.
(15) Sheng, N.; Boyce, M. C.; Parks, D. M.; Rutledge, G. C.; Abes, J. I.; Cohen, R. E. *Polymer* **2004**, *45*, 487.
(16) Berlin, A. A.; Oshmyan, V. G.; Patlazhan, S. A.; Timan, S. A.; Shamaev, M. Yu.; Khokhlov, A. R. *Polym. Sci. A* **2006**, *48*, 198.
(17) Manevitch, O. L.; Rutledge, G. C. *J. Phys. Chem. B* **2004**, *108*, 1428.
(18) Essmann, U.; Perera, L.; Berkowitz, M. L.; Darden, T.; Lee, H.; Pedersen, L. G. *J. Chem. Phys.* **1995**, *103*, 8577.
(19) Lemak, A. S.; Balabaev, N. K. *Mol. Simul.* **1995**, *15*, 223.
(20) Lemak, A. S.; Balabaev, N. K. *J. Comput. Chem.* **1996**, *17*, 1685.
(21) Berendsen, H. J. C.; Postma, J. P. M.; van Gunsteren, W. F.; DiNola, A.; Haak, J. R. *J. Chem. Phys*. **1984**, *81*, 3684.
(22) Wardle, R.; Brindley, G. W. *Am. Mineral.* **1972**, *57*, 732.
(23) Lee, J. H.; Guggenheim, S. *Am. Mineral.* **1981**, *66*, 350.
(24) Nye, J. F. *Physical Properties of Crystals*; Oxford University Press: London, 1957.
(25) Allen, M. P.; Tildesley, D. J. *Computer Simulation of Liquids*; Clarendon Press: Oxford, U.K., 1987.
(26) Lekhnitskiy, S. G. *Anisotropic Plates*; Gostehteorizdat: Moscow, 1957.
(27) Chen, B.; Evans, J. R. G. *Scr. Mater*. **2006**, *54*, 1581.